PROCEEDINGS, 47th Workshop on Geothermal Reservoir Engineering
Stanford University, Stanford, California, February 7-9, 2022
SGP-TR-223

Overview and Preliminary Results from the WHOLESCALE project at San Emidio, Nevada, U.S.

Kurt L. FEIGL, Sui TUNG (1), Hao GUO (1), Erin CUNNINGHAM (1), Jesse HAMPTON (1), Samantha J. KLEICH (1), Ben JAHNKE (1), Ben HEATH (1), Collin Roland (1), Matthew FOLSOM (2), John AKERLEY (2), Matteo CUSINI (3), Chris SHERMAN (3), Ian WARREN (5), Corné KREEMER (4), Hiroki SONE (1) Michael A. CARDIFF (1), Neal E. LORD (1), Clifford H. THURBER (1), and Herbert F. WANG (1)

(1) University of Wisconsin-Madison, Department of Geoscience, Madison, WI, United States;
(2) Ormat Technologies Inc., Reno, NV, United States;
(3) Lawrence Livermore National Laboratory, Livermore, CA, United States;
(4) University of Nevada Reno, NV, United States;
(5) National Renewable Energy Lab. (NREL), Golden, CO, United States.

feigl@wisc.edu

Keywords: WHOLESCALE, San Emidio, EGS, GPS, INSAR, FEM

ABSTRACT

The WHOLESCALE acronym stands for Water & Hole Observations Leverage Effective Stress Calculations and Lessen Expenses. The goal of the WHOLESCALE project is to simulate the spatial distribution and temporal evolution of stress in the geothermal system at San Emidio in Nevada, United States. To reach this goal, the WHOLESCALE team is developing a methodology that will incorporate and interpret data from four methods of measurement into a multi-physics model that couples thermal, hydrological, and mechanical (T-H-M) processes over spatial scales ranging from the diameter of a borehole (~0.1 m) to the extent of the entire field (~10 km) and temporal scales ranging from the duration of a microseismic event (~1 second) to the typical lifetime of a producing field (3 decades). The data sets include observations from geology, seismology, drilling, geodesy, and hydrology.

The WHOLESCALE team is taking advantage of the perturbations created by changes in pumping operations to infer temporal changes in the state of stress in the geothermal system. This rheological experiment is based on the key idea that increasing pore-fluid pressure reduces the effective normal stress acting across preexisting faults. The work plan includes: (1) measuring rock-mechanical material properties in the laboratory, (2) manipulating the stress field via hydraulic and thermal methods, (3) measuring the resulting response by geophysical methods, and (4) calculating the stress, strain, pressure, and temperature in the geothermal system using an open-source, numerical simulator named GEOSX. To interpolate and interpret these rich data sets, GEOSX uses the finite-element method to solve the coupled differential equations governing the physics of a fractured, poroelastic medium under stress. The study site at San Emidio includes a volume with length of ~6 km, width ~5 km, and depth ~2 km. In this paper, we provide a snapshot of work in progress, including the highlights listed in the conclusions below. The work presented herein has been funded in part by the Office of Energy Efficiency and Renewable Energy (EERE), U.S. Department of Energy, under Award Numbers DE-EE0007698 and DE-EE0009032.

INTRODUCTION

The San Emidio geothermal area is located ~100 km north of Reno Nevada in the northwestern Basin and Range province, as described previously [*Rhodes et al.*, 2010; *Eneva et al.*, 2011; *Rhodes et al.*, 2011; *Faulds*, 2014; *Teplow and Warren*, 2015; *Reinisch et al.*, 2019a; *Reinisch et al.*, 2019b; *Warren et al.*, 2019; *Feigl et al.*, 2020; *Folsom et al.*, 2020; *Folsom et al.*, 2021]. The San Emidio geothermal system occupies a right step in a North-striking, West-dipping, normal fault zone. Minor dilation and high fault density within the right step likely produce the permeability necessary for deep fluid circulation [*Eneva et al.*, 2011]. Power was first produced in 1987 with a 3.6-MW binary plant, and average production increased to 9 MW (net) following commissioning of a new power plant in 2012. Production has ranged from less than 190 L/s to more than 280 L/s at temperatures of 140–148˚C. Drilling, geological, geophysical, and geochemical data sets collected since the 1970s help constrain controls on the geothermal resource and the structural setting (Figure 1 and Figure 2).

The geothermal field at San Emidio provides an ideal laboratory for understanding subsurface stress. The data collected over more than 20 years of operating experience characterize the structure, temperature, microseismicity, and permeability, all of which are directly associated with changes in the stress within the geothermal system. The data sets include historic drilling records, magnetotelluric resistivity, seismic reflection imaging, passive seismic emission tomography (PSET), microseismicity analysis, and gravimetric surveys.

Our WHOLESCALE project is funded by a peer-reviewed grant awarded by the Geothermal Technologies Office of the U.S. Department of Energy. The goal of the WHOLESCALE project is to simulate the spatial distribution and temporal evolution of stress in a geothermal system. To reach this goal, the WHOLESCALE team is developing a methodology to incorporate and interpret data from four methods of measurement into a multi-physics model that couples thermal, hydrological, and mechanical (T-H-M) processes over spatial scales ranging from the diameter of a borehole (~0.1 m) to the extent of the entire field (~10 km) and temporal scales ranging from the duration of a microseismic event (~1 second) to the typical lifetime of a producing field (3 decades).

DATA AND METHODS

The WHOLESCALE team is taking advantage of the perturbations created by pumping operations to infer temporal changes in the state of stress in the geothermal system. This rheological experiment is based on the key idea that increasing pore-fluid pressure reduces the effective normal stress acting across preexisting faults. Accordingly, the WHOLESCALE team is analyzing four types of observational data at San Emidio, measuring material properties of San Emidio rock samples in our laboratory, and synthesizing with a multiphysics T-H-M modeling code named GEOSX that has been developed at Lawrence Livermore National Laboratory.

Observations

(1) Seismology can determine the locations and focal mechanisms of microseismic events. Seismic tomography — when combined with density models estimated from gravimetric surveys — also provides constraints on material properties such as Poisson's ratio and shear modulus. We are currently analyzing seismic data acquired in December 2016 [*Warren et al.*, 2018; *Warren et al.*, 2019; *Thurber et al.*, 2021]. A dense array of 3-component seismic instruments will be deployed over the same area during a planned shutdown of the production wells in April 2022.

(2) Borehole image logs can observe failures in the formation surrounding the well bore to constrain the magnitude and orientation of stress [e.g., *Zoback*, 2007]. Wireline logging will include: (a) electrical logs of porosity, density, resistivity; (b) image logs; and (c) sonic logs. We are also using regional indicators of stress to constrain the far-field boundary conditions, as described at this meeting [*Jahnke et al.*, 2022].

(3) Geodesy measures deformation of the ground surface. Two continuously operating GPS stations, SEMS and SEMN, have been installed on monuments attached to idle wellheads within the geothermal field at San Emidio. A third GPS station, named GARL, is located outside the geothermal area in the mountain range to the northeast of the power plant to provide a stable reference point. We analyze the GPS data to calculate daily measurements of (relative) position coordinates in three dimensions that can be modeled as time series of displacement [*Kreemer et al.*, 2020; *Blewitt et al.*, 2018]. Interferometric Synthetic Aperture Radar (InSAR) data also measures ground deformation. We are analyzing InSAR data collected by several satellite missions. One data set consists of radar images acquired monthly beginning in 2019 by the TerraSAR-X [*Pitz and Miller*, 2010] and TanDEM-X [*Krieger et al.*, 2007] satellite missions operated by the German Space Agency (DLR). We are also analyzing InSAR data from the SENTINEL-1 satellite mission [*Salvi et al.*, 2012] operated by the European Space Agency (ESA). These data sets cover the site from late 2014 through the present. To analyze these data, we are developing two high-throughput workflows using HT-Condor [*Reinisch*, 2019]. For the TerraSAR-X and TanDEM-X data, the workflow uses the GMT-SAR processing software [*Sandwell et al.*, 2011]. For the data acquired by the SENTINEL missions, we use the Interferometric synthetic aperture radar Scientific Computing Environment (ISCE) that is being developed by colleagues at NASA's Jet Propulsion Laboratory [*ISCE*, 2020].

(4) Hydrology measures pressure and temperature in multiple boreholes to quantify the propagation of fluid-pressure fronts and changes to effective normal stress. Existing evidence from San Emidio indicates that the subsurface is highly heterogeneous. We are working to test the hypothesis that the fluid-flow pathways are controlled by faults, as we inferred at Brady Hot Springs during the PoroTomo project [*Patterson*, 2018]. At San Emidio, we are using analytical and numerical models to match the histories of pressure and flow. We have developed a model using an analytic solution for drawdown [*Theis*, 1935]. This solution simulates the 2-dimensional pressure propagation along a hypothetical permeable plane. We estimate hydrologic transmissivity T [m^2/s] and storativity S [-] to optimize the fit to the pressure signals observed at two observation wells at San Emidio. We consider three cases, fitting data from well OW8 first, then well OW9, and finally both wells in combination. In all three cases, the modeled pressure changes agree with the observed values within 2 kPa, equivalent

to approximately 20 cm of water. That the estimated values of *T* and *S* differ between the two wells argues for spatial heterogeneity in these hydrologic properties.

Modeling

To interpolate, interpret, synthesize, and simulate these rich data sets, the WHOLESCALE team will solve the coupled differential equations governing the physics of a fractured, poroelastic medium under stress. We will perform thermo-hydro-mechanical (T-H-M) coupled modeling using a numerical simulator named GEOSX [*Liu et al.*, 2018]. Using a combination of the finite-element and finite-volume methods, the GEOSX code solves the coupled differential equations governing the flow of fluid and heat as well as the mechanics of the medium deforming under stress. The resulting solution includes the complete stress tensor σ_{ij} as a function of time *t* at every location *(x, y, z)* in a large 3-dimensional mesh of the study volume.

Laboratory

In configuring the T-H-M models, the WHOLESCALE team seeks to honor the geologic structure and its material properties. The rock mechanical properties (e.g., Poisson's ratio, density, Young's modulus) are measured in samples via laboratory experiments as described at this meeting [*Kleich et al.*, 2022] To account for heterogeneities in mechanical properties over the scale of the reservoir, the WHOLESCALE team plans to extend the values measured in the lab with information from the borehole logs and the geologic model [*Rhodes*, 2011] using data-science techniques [e.g., *Bayuk et al.*, 2008].

RESULTS

The geodetic data show subsidence around the production wells at rates of several millimeters per year with respect to the mountain range to the east of the power plant (Figure 3, Figure 4, Figure 5, Figure 6). The deformation pattern observed at San Emidio is more subtle and more complex than that at Brady [*Reinisch et al.*, 2018; *Reinisch et al.*, 2020].

Tomographic models of seismic velocity (Figure 8) show contrasts that are consistent with normal faults striking north-south and dipping westward (Figure 9).

The locations of microseismic events have been determined from seismic data recorded by a local seismic network in 2016 (Figure 10). Many of the events appear to occur on or near normal faulting structures in the geologic model (Figure 7 and Figure 8).

The focal mechanisms of microseismic events have also been determined from seismic data recorded by a local seismic network in 2016. Several of the events cluster on a plane dipping westward (Figure 9). The focal mechanisms are consistent with a normal-faulting regime with the maximum horizontal stress oriented approximately North-South (Figure 11 and Figure 12).

As shown in Figure 13, laboratory testing of rock samples indicates that none of the lithologic units tested (i.e., TrJn, Tpb', and Tss) possess any significant observations of anisotropy and/or heterogeneities at the specimen scale. Measurements of seismic velocity at different orientations in the same sample agree to within 250 m/s, which is not an appreciable difference considering the average velocity of these specimens is around 4,000 m/s. Although the presence of fabric is indicated in thin sections made from these rock samples, the fabric does not contribute to measurable anisotropy during radial velocity testing. Therefore, most samples are classified as isotropic. This information will be used when further analyzing mechanical and poroelastic data from tested rock specimens.

DISCUSSION

By analyzing the data streams at geothermal fields, we can take advantage of the perturbations created by pumping operations to infer temporal changes in the state of stress in the geothermal system. For example, the PoroTomo experiment was conducted at the geothermal field at Brady Hot Springs, Nevada [*Feigl and Parker*, 2019]. There, a scheduled cessation of both production and injection pumping produced fluid pressure changes as large as 150 kPa (roughly equivalent to 15 m of water) [*Patterson et al.*, 2017] that are associated with microseismic events with magnitude less than M 2 [*Cardiff et al.*, 2018]. At Brady, these authors observed that "shutdowns in pumping for plant maintenance correlate with increased microseismicity" [*Cardiff et al.*, 2018]. Following these authors, we hypothesize that "extraction of fluids inhibits fault slip by increasing the effective [normal] stress on faults; in contrast, brief pumping cessations represent times when effective [normal] stress is decreased below its long-term average, increasing the likelihood of microseismicity" [*Cardiff et al.*, 2018].

Similar phenomena have been observed at San Emidio. In the month of December 2016, more than 100 discrete microseismic events occurred as the power plant and pumping were shut down for maintenance and subsequently restarted [*Warren et al.*, 2018]. These events are related temporally to the geothermal brine recovering during shutdown (Figure 14). Their locations cluster around the producing wells, as shown in Figure 15. The location and timing of the events are consistent with 2-dimensional analytic models that show increased fluid pressure over length scales of the order of several kilometers from the production wells and temporal scales of the order of tens of hours from the cessation of production and injection (Figure 16, Figure 17, Figure 18).

Observations elsewhere also indicate that anthropogenic perturbations to hydrological systems can alter the state of stress sufficiently to trigger seismic slip on pre-existing faults [e.g., *Raleigh et al.*, 1976; *Majer et al.*, 2007; *Ellsworth*, 2013; *Segall and Lu*, 2015]. Similarly, extracting and injecting brine out of and into geothermal fields can also induce seismicity, especially in enhanced geothermal systems (EGS) [*Majer et al.*, 2007; *Brodsky and Lajoie*, 2013; *NRC*, 2013; *Kwiatek et al.*, 2015; *McGarr et al.*, 2015; *Trugman et al.*, 2016].

Such induced seismicity is caused by changes to the state of stress in and around the geothermal reservoir. Indeed, we hypothesize that increasing pore-fluid pressure reduces the effective normal stress acting across preexisting faults and induces microseismic events.

The operators of the power plant are planning to suspend normal operations for several days in April 2022. During this time interval, pumping will cease at all production and injection wells. We expect microseismic events to occur in a manner like that observed in December 2016. Specifically, Table 1 lists the variables describing microseismic events during temporary shutdowns at San Emidio, as observed in December 2016 and expected in April 2022.

To determine the magnitude of the microseismic events detected in December 2016, we draw an inference from two observations in a logical syllogism. The first observation is that during the time interval $t \in [7, 12]$ December 2016, no events were detected by either of the regional seismic networks, as listed in their catalogues: U.S. Geological Survey [USGS] and Northern California Earthquake Data Center [NCEDC].

The second observation is that during the time interval $t \in [2013/01/01, 2020/12/31]$, the magnitude of completeness is M 1.3. To determine this value, we have examined Gutenberg-Richter plots for the comprehensive (de-clustered) seismicity catalog "ComCat". [USGS, 2017] Considering a sample of $n = 100$ events nearest (< 42 km from) the power plant at San Emidio, we find that the curve showing the logarithm of the cumulative number of events below a given magnitude begins to deviate from a straight line at M 1.3. Considering a sample of $n = 200$ events nearest (< 80 km from) the power plant at San Emidio, we also find a completeness magnitude of M 1.3,

By combining the two observations, we infer that the events detected by the local network in December 2016 have magnitude less than M 1.3.

Table 1. Variables describing microseismic events during temporary shutdowns at San Emidio, as observed in December 2016 and expected in April 2022.

Variable	Lower bound	Upper bound	Notes
Timing: hours after cessation of production and injection.	7.4 hours	12.1 hours	Bounds represent 25th and 75th percentiles, respectively. Seismic data were recorded only for ~40 hours following resumption of production in 2016.
Location (radial distance from nearest production well)	243 m	395 m	Bounds represent 25th and 75th percentiles, respectively.
Elevation above WGS84 geoid	588 m	794 m	Bounds represent 25th and 75th percentiles, respectively.
Magnitude	Not defined	M 1.3	Completeness magnitude of catalog.

CONCLUSIONS

The study site at San Emidio includes a volume with length of ~6 km, width ~5 km, and depth ~2 km. At each point within a mesh of this volume, the resulting numerical solution will determine the complete stress tensor as a function of time as well as its sensitivity to perturbations in the input parameters. The numerical GEOS solution will also calculate modeled values for each of the four types of observable quantities. By optimizing the goodness of fit between the observations and the modeled value calculated by the GEOSX simulator, the WHOLESCALE methodology is currently seeking the model configuration that best fits the data while assessing the uncertainty of the associated reservoir parameters. The result will be a reliable simulation of the spatial distribution and temporal evolution of the full stress tensor $\sigma_{ij}(t, x, y, z)$ at San Emidio.

ACKNOWLEDGMENTS

We thank the following individuals for skillful assistance in the field: Joe Pavone, Clifford Reed, Alan Pinuelas, Zack Young, Quaid Ricks, and Chris Gates.

We thank Bill Barker and Charlie Stevens at Microseismic Inc. for helpfully providing information regarding the seismic survey in December 2016.

We gratefully acknowledge support from the Weeks family to the Department of Geoscience at the University of Wisconsin-Madison.

Seismicity catalogs for this study were accessed through the Northern California Earthquake Data Center (NCEDC), doi:10.7932/NCEDC.

We acknowledge image data acquired by the TerraSAR-X [*Pitz and Miller*, 2010] and TanDEM-X [*Krieger et al.*, 2007] satellite missions operated by the German Space Agency (DLR). These data were used under the terms and conditions of Research Project RES1236. Image data were also acquired by the SENTINEL-1 satellite mission [*Salvi et al.*, 2012] operated by the European Space Agency (ESA).

Some of the figures in this paper were generated using Leapfrog Software, a trademark of Seequent Limited.

The work presented herein has been funded in part by the Office of Energy Efficiency and Renewable Energy (EERE), U.S. Department of Energy, under Award Numbers DE-EE0007698 and DE-EE0009032.

FIGURES

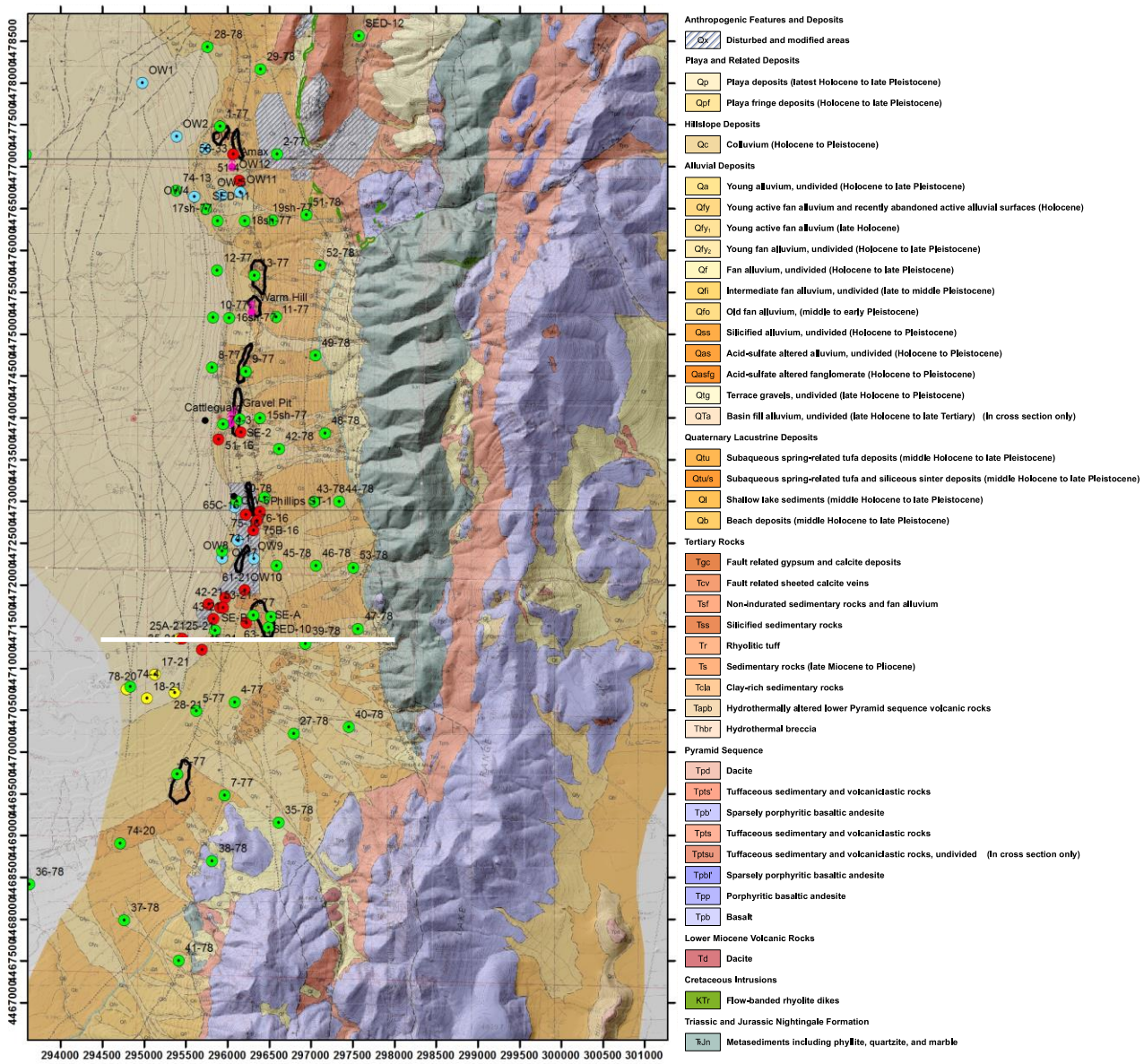

Figure 1. Geologic map of San Emidio [*Rhodes,* 2011], showing lithology [*Rhodes et al.*, 2011], and transect (white line segment). Coordinates are easting and northing in meters in the Universal Transverse Mercator (UTM) cartographic projection. Circles show wells.

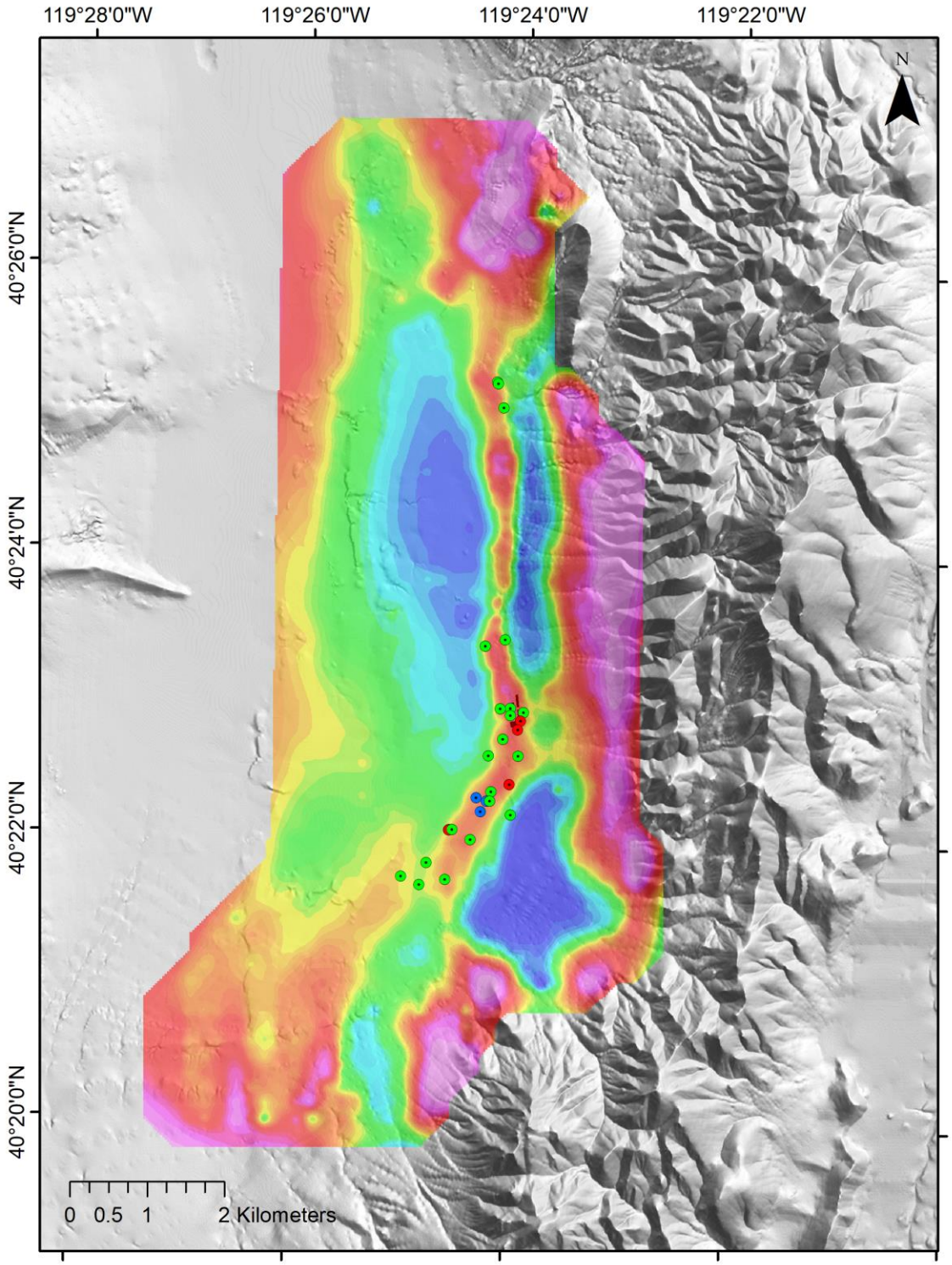

Figure 2. Map of vertical derivative of complete Bouguer gravity anomaly (colors), reduced with density of 2.3 g/cm3 and gridded at 30 m [*Folsom et al.*, 2020]. Gray shading shows topographic relief. Black square shows power plant.

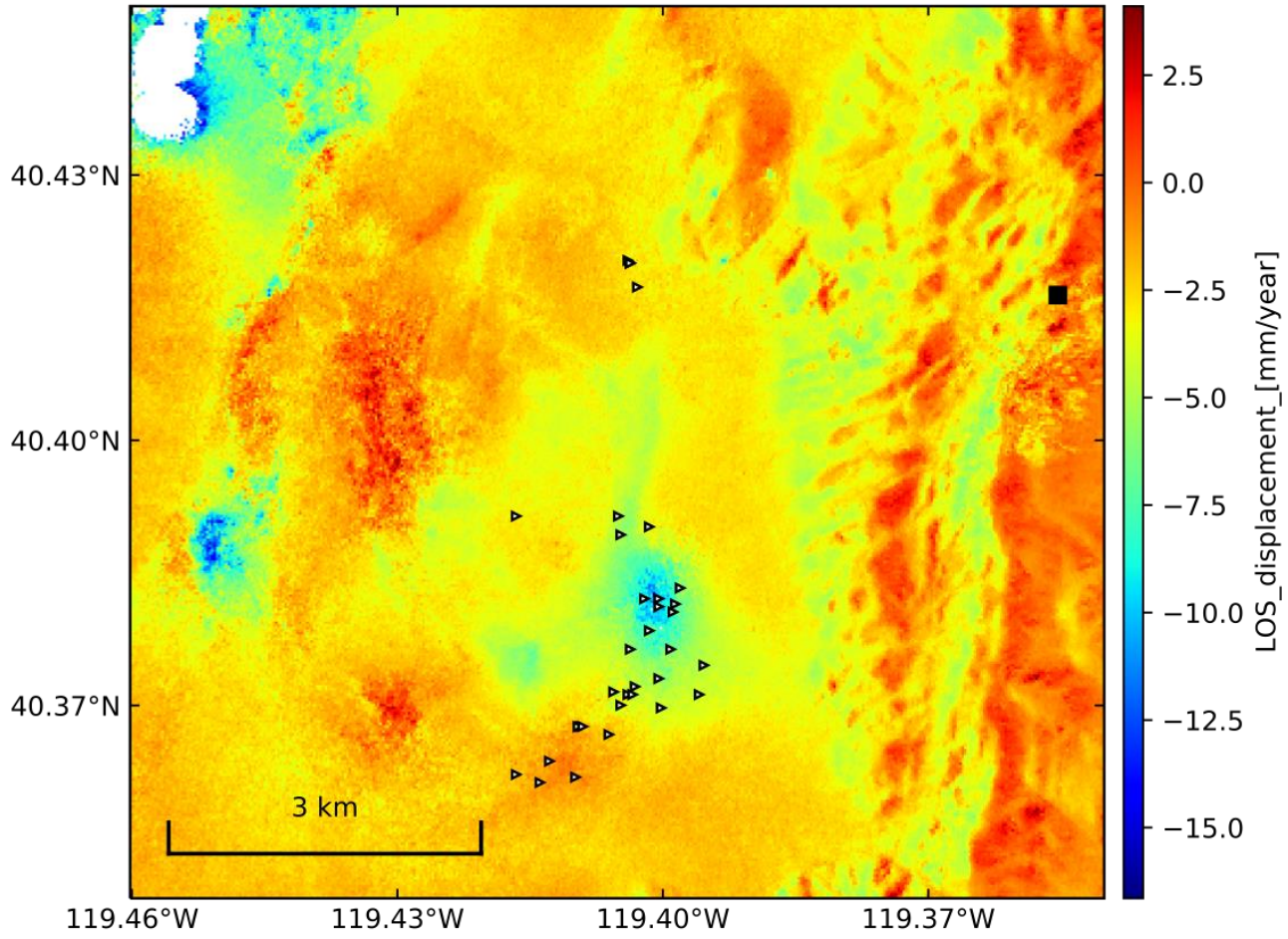

Figure 3. Map of deformation field showing the mean rate of line-of-sight (LOS) displacement from InSAR data spanning 2018 through 2020. The mean LOS displacement rate was estimated from a stack of unwrapped interferograms acquired by the Sentinel 1A and 1B satellite missions in Track 144 using ISCE [*ISCE*, 2020] and MintPy [*Yunjun et al.*, 2019] without accounting for atmospheric effects.

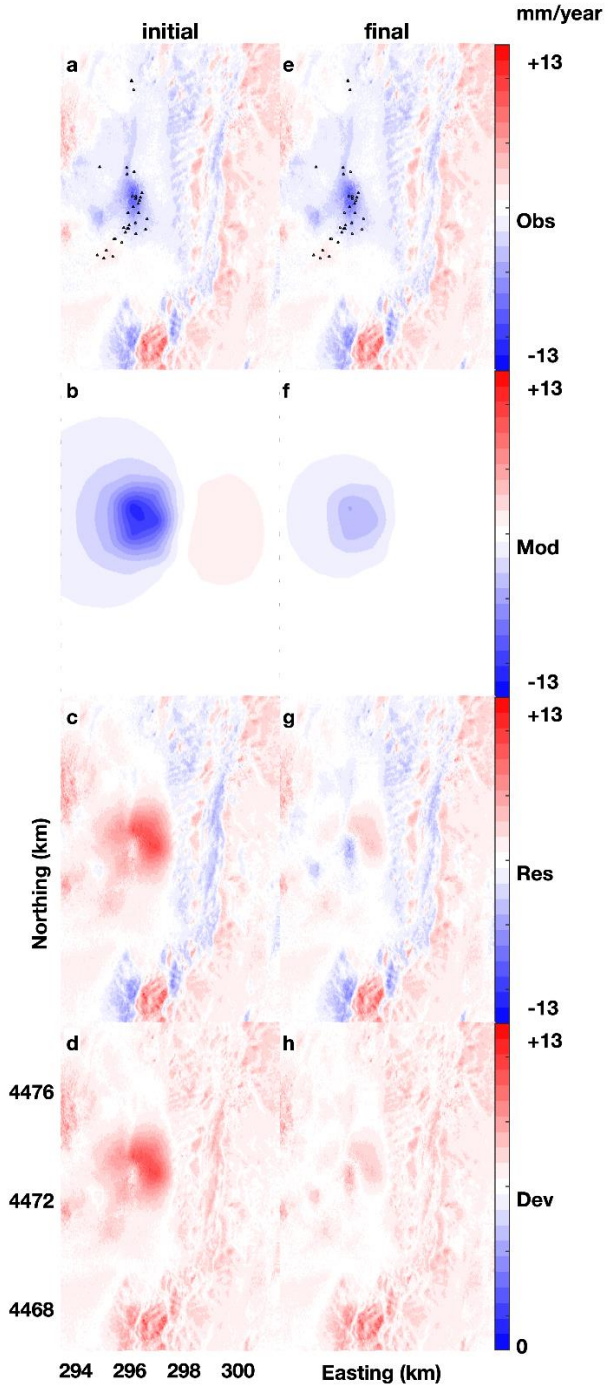

Figure 4. Deformation fields in terms of the rate of line-of-sight (LOS) displacement from InSAR data spanning 2018 through 2020 showing: (a, e) observed LOS displacement rate estimated from a stack of unwrapped interferograms acquired by the Sentinel 1A and 1B satellite missions in Track 144 using ISCE and MintPy without accounting for atmospheric effects; (b, f) modeled LOS displacement rate, (c, g) residual between observed and modeled; and (d, h) absolute value of residuals. Left column, including panels a, b, c, and d show initial estimate of model parameters. Right column, including panels e, f, g, and h, shows final estimate of model parameters. Coordinates are easting and northing [km] in Universal Transverse Mercator (UTM) projection zone 11N, WGS 84.

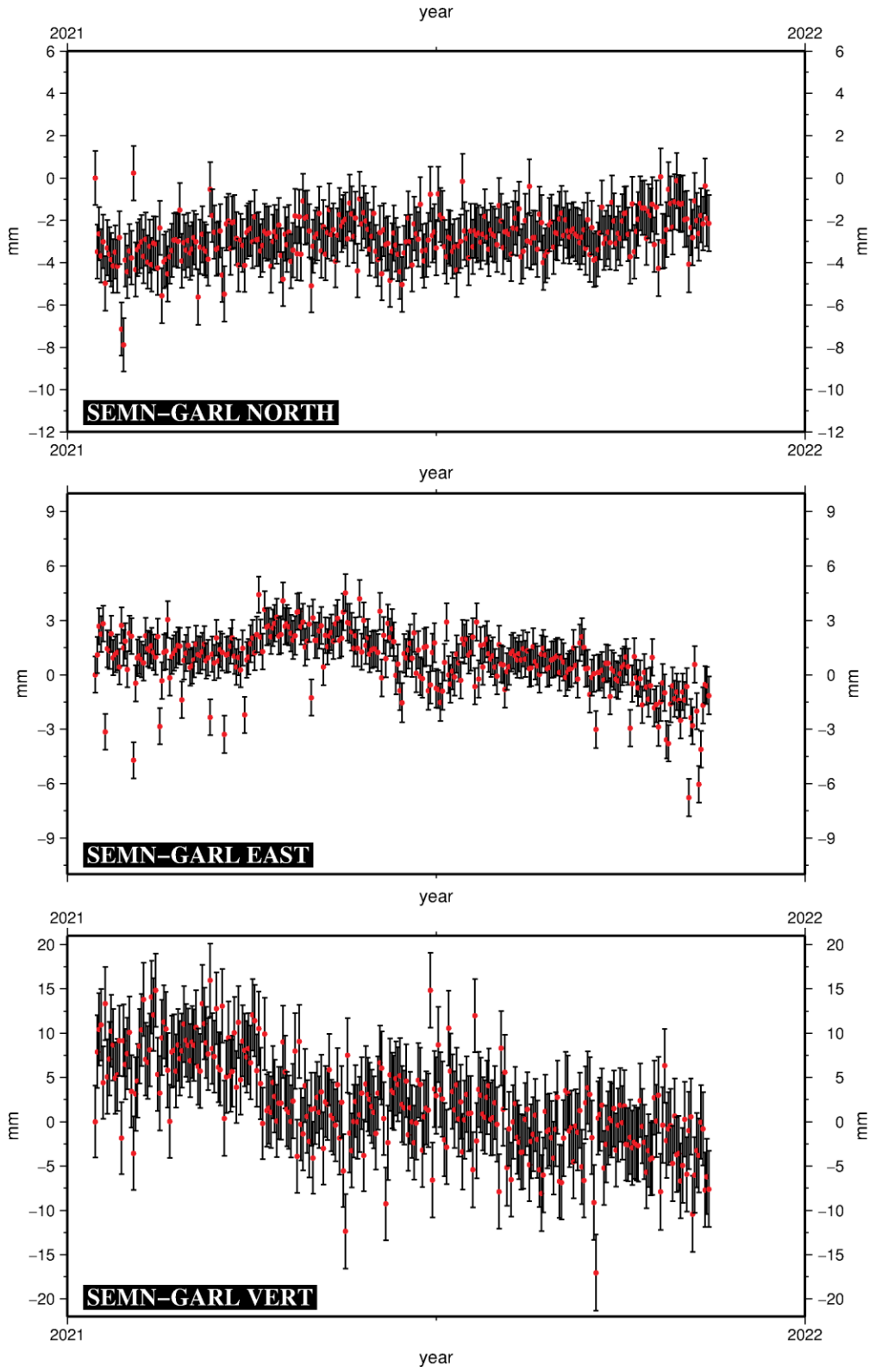

Figure 5 Time series of daily estimates of position of GPS station SEMN relative to GARL. Data analysis by Nevada Geodetic Laboratory.

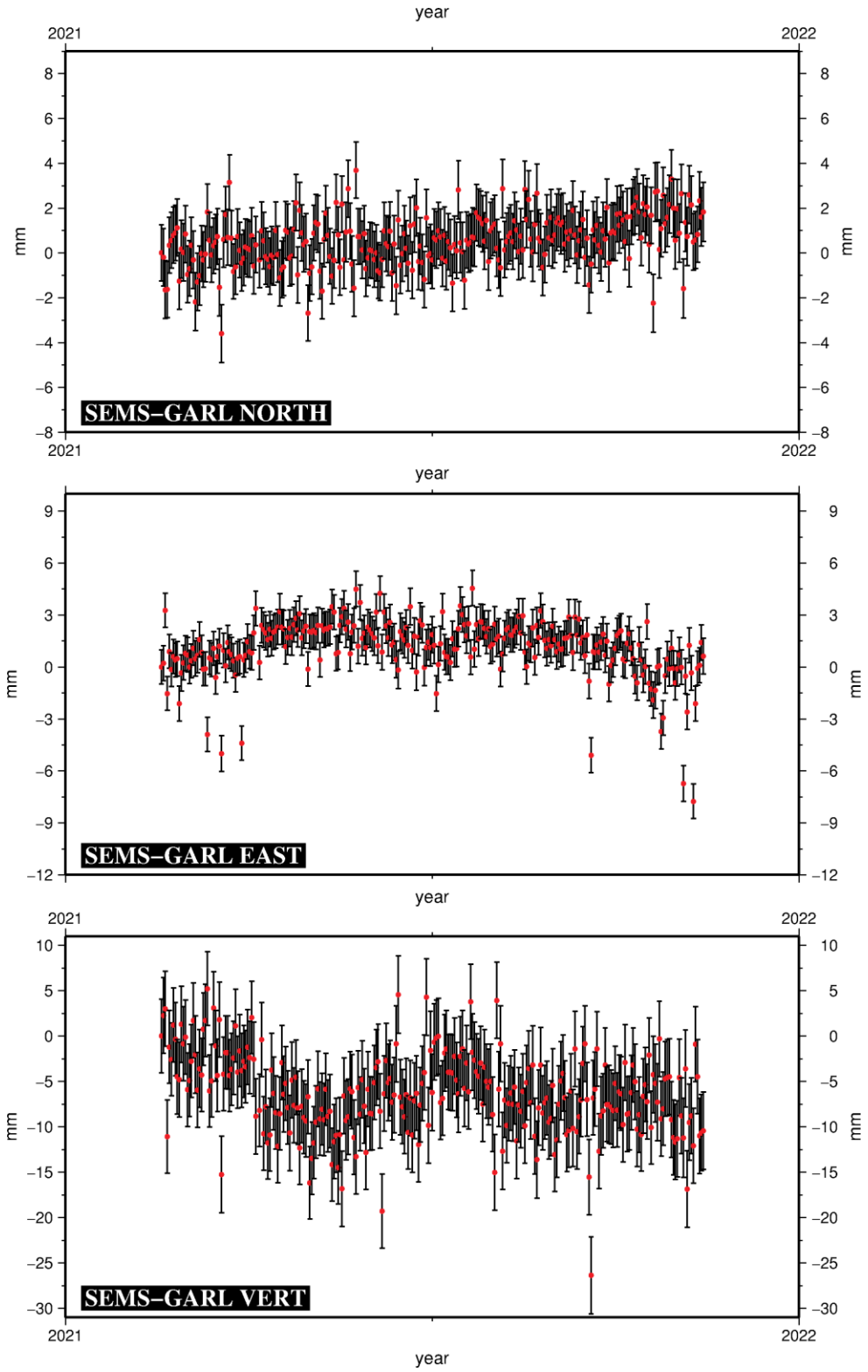

Figure 6. Time series of daily estimates of position of GPS station SEMS relative to GARL. Data analysis by Nevada Geodetic Laboratory.

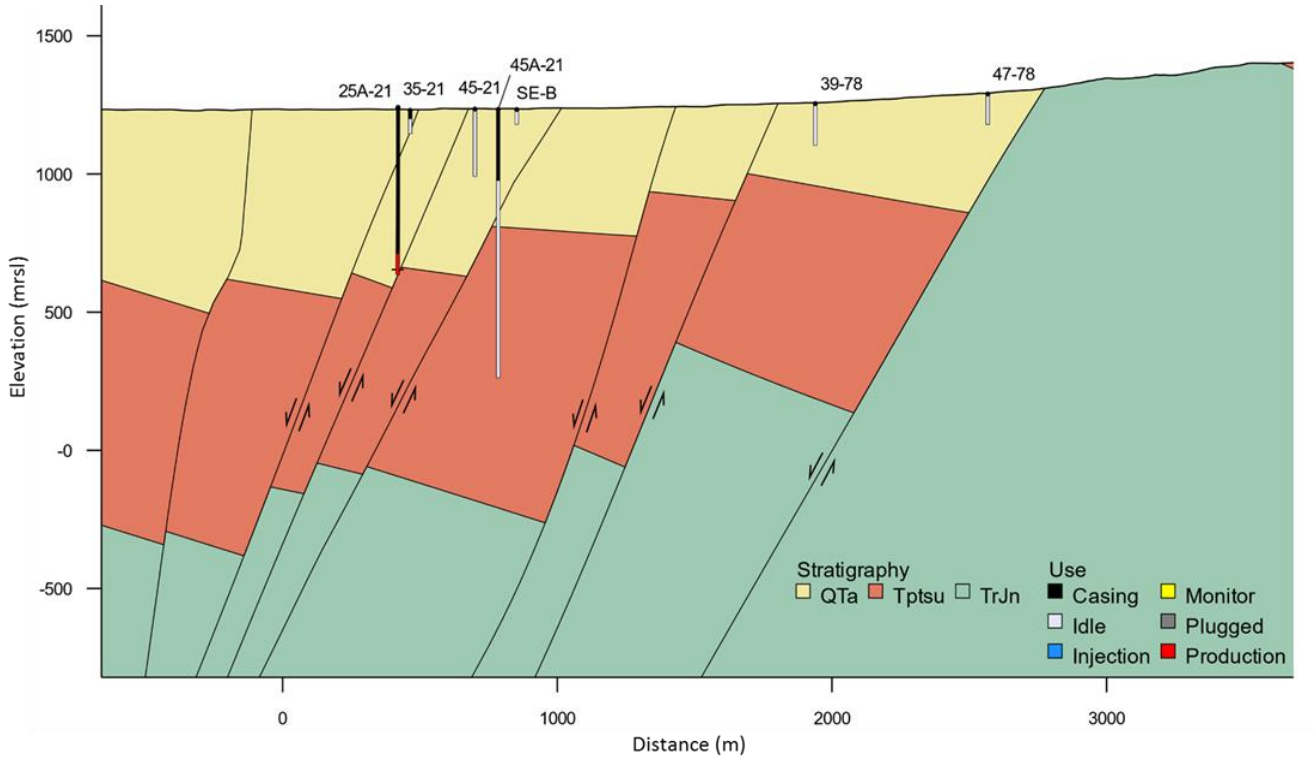

Figure 7. Geologic cross section, showing primary lithologic units, wells, and faults. Vertical plane is an E-W transect at Northing coordinate 4471,000 m (white segment in Figure 1). Elevation relative to sea level in meters [*Rhodes*, 2011; *Rhodes et al*., 2011].

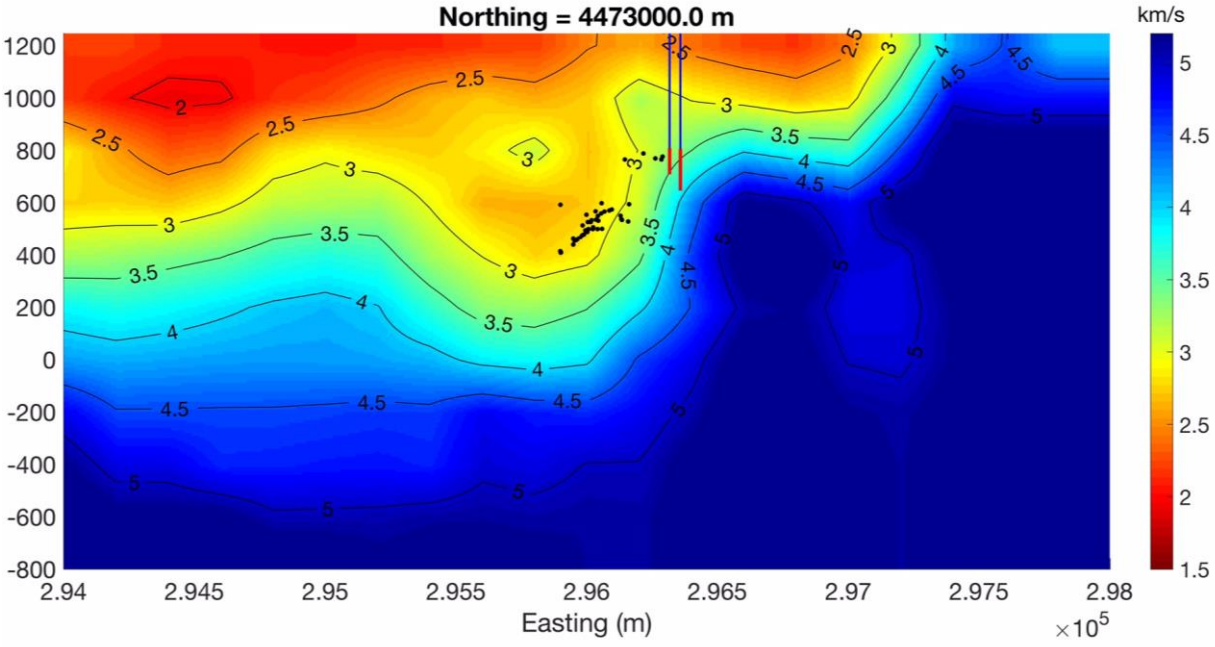

Figure 8. Seismic cross section, showing P-wave velocity in km/s (colors) and microseismic events (black circles). Vertical plane is an E-W transect at Northing coordinate 4473,000 m (i.e., 2000 m north of the transect shown in Figure 7 and mapped as a white line in Figure 1). Vertical coordinate Z corresponds to meters above WGS 84 geoid (masl). Seismic data from 2016 survey [*Warren et al.*, 2018]. Tomographic analysis [*Thurber et al*., 2021].

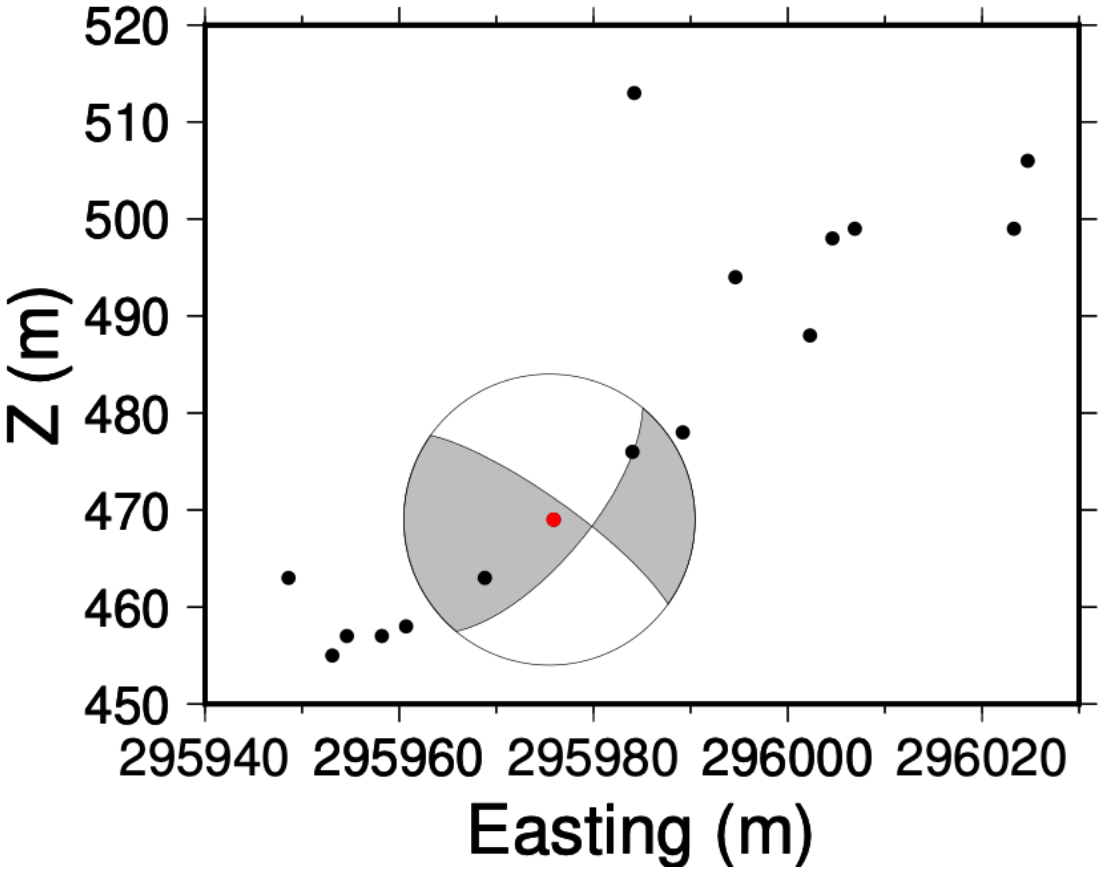

Figure 9. Vertical cross section showing a focal mechanism and the locations of microseismic events in December 2016 clustering on an west-dipping plane [*Thurber et al.*, 2021]. Vertical coordinate Z corresponds to meters above WGS 84 geoid (masl). Microseismic events shown here are located at UTM northing coordinates between 4472,970 m and 4473,030 m.

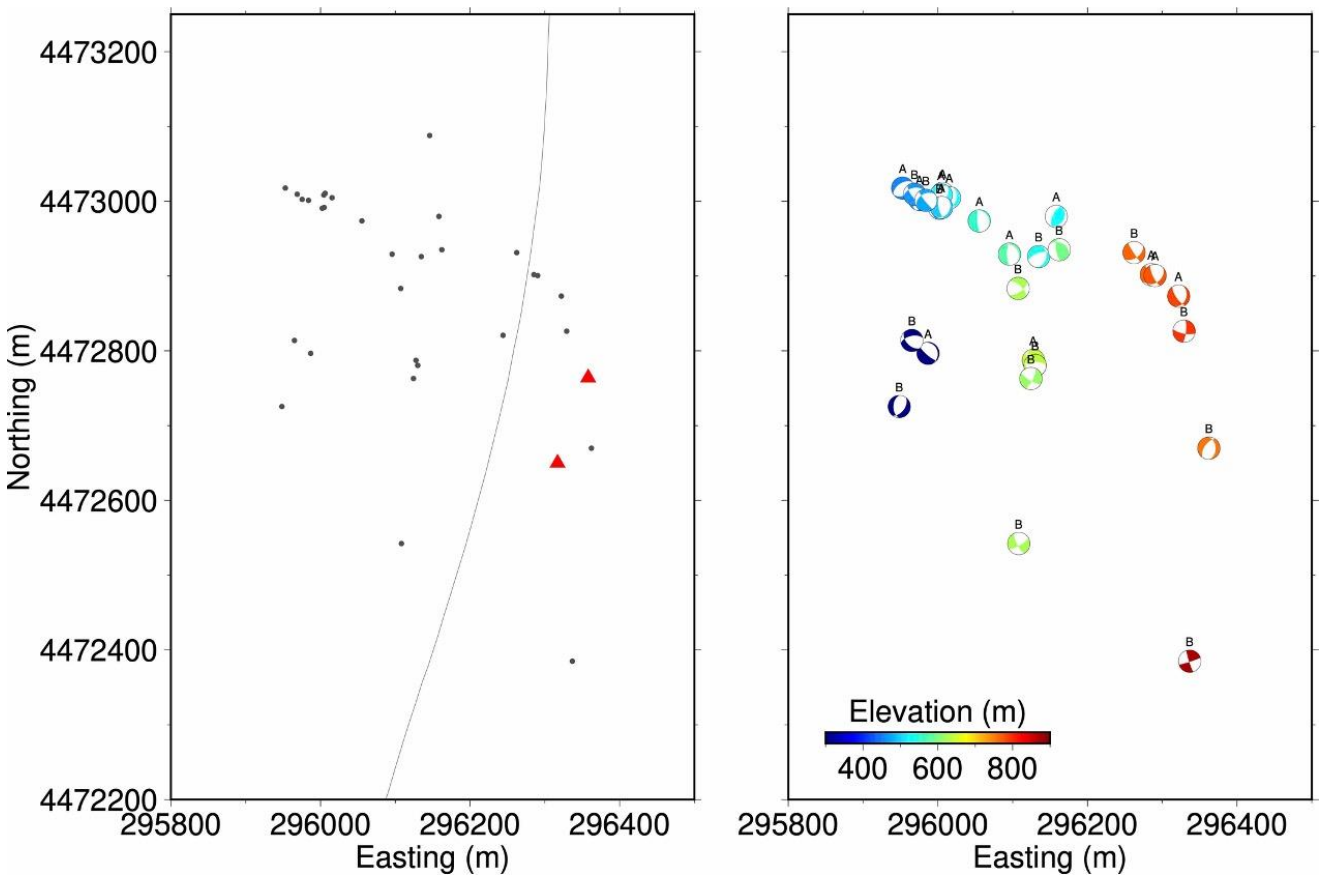

Figure 10. Maps showing locations of microseismic events (left) and focal mechanisms (right) determined from seismic data recorded in December 2016 [*Thurber et al.*, 2021]. Only focal mechanisms with quality A or B [*Hardebeck and Shearer*, 2002] are shown. Production wells 75B-16 (northern red triangle) and 76-16 (southern red triangle). Thin black line indicates surface trace of east-dipping normal fault named the "Basin Bounding Fault B1" [*Rhodes*, 2011; *Rhodes et al.*, 2011; *Folsom et al.*, 2020; *Folsom et al.*, 2021].

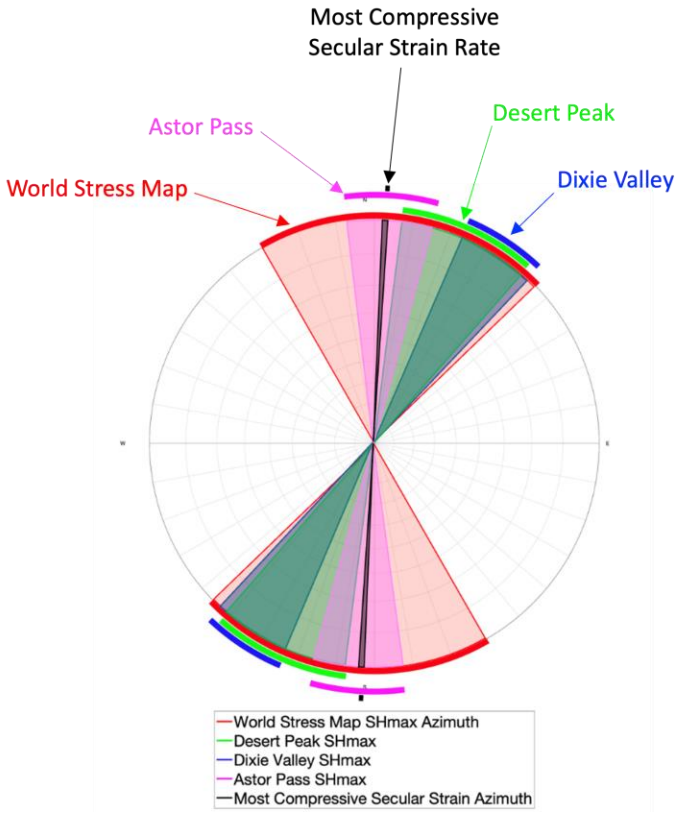

Figure 11. Summary of regional observations of stress orientation, showing the azimuth maximum horizontal compressive stress SHmax azimuths. Red shaded regions indicate range of SH, max azimuths from observations documented in the World Stress Map (Heidbach et al., 2018). Green, blue, and pink shaded regions indicate ranges of SH, max azimuths from wellbore indicators from Desert Peak (Hickman & Davatzes, 2010), Dixie Valley (Hickman et al., 1998), and Astor Pass (Siler et al., 2016), respectively. Black shaded region indicates the direction of the most compressive secular strain azimuth, or direction of maximum compressive strain rate (Kreemer et al., 2014). Figure and caption [*Jahnke et al.*, 2022].

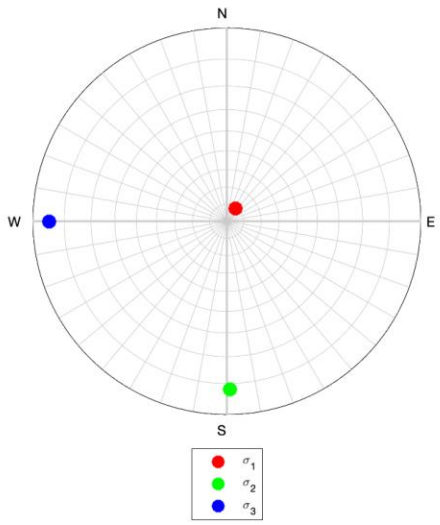

Figure 12. Reservoir stress state estimated by iterative joint inversion [*Vavryčuk*, 2014] from all focal mechanism data from the plant shutdown in December 2016 [*Thurber et al.*, 2021]. The red, green, and blue markers correspond to the orientations of σ_1, σ_2, and σ_3, respectively, estimated from focal mechanisms. Figure and caption [*Jahnke et al.*, 2022].

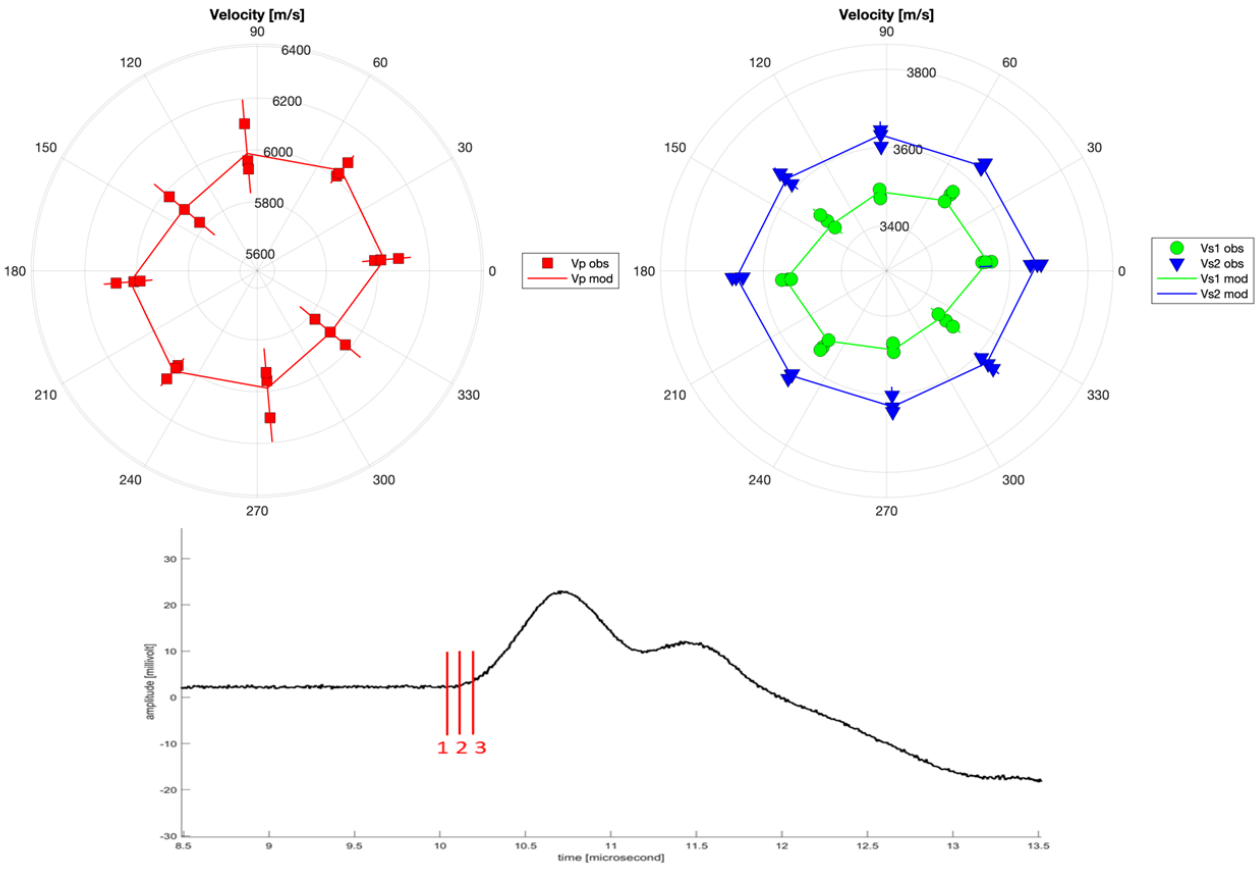

Figure 13. Example polar plots of velocity picks from TrJn (metasedimentary) sample collected at San Emidio. Observed P-wave velocity picks indicated by red squares (top left). Observed S1-wave velocity picks indicated by green circles and S2-wave velocity picks indicated by blue triangles (top right). The straight lines connecting the observed velocity values at each orientation is the best fitting curve through the three points and is not based on predictions. The three points at each orientation on the polar plots corresponds to the three different locations for velocity picks indicated in red on the example P-wave seismogram (bottom). The range of error is based on these three velocity picks. This sample is classified as isotropic due to velocity values not varying by more than 250 m/s and for that reason, creates the relatively circular shape depicted on the polar plots. Figure and caption [*Kleich et al.*, 2022].

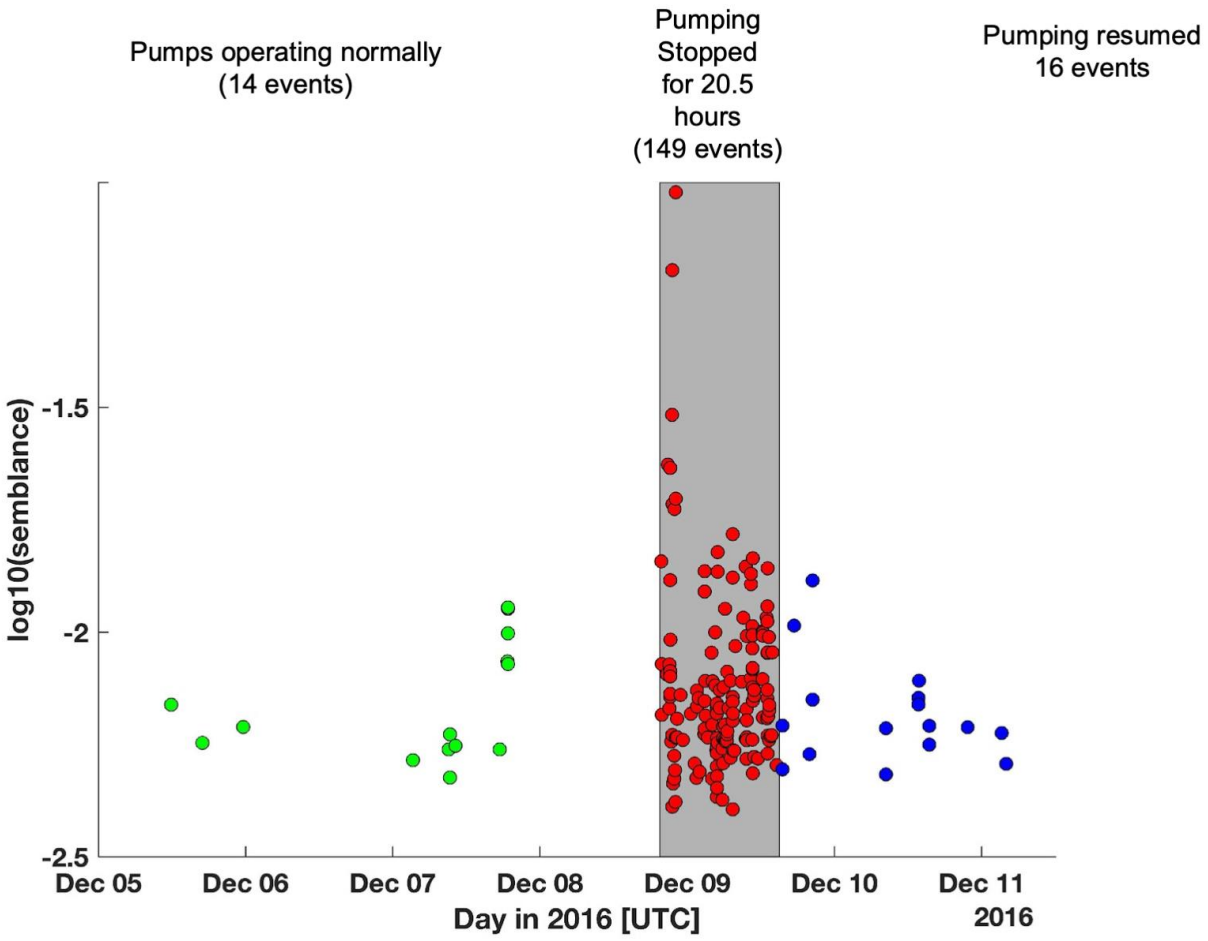

Figure 14. Timeline of microseismic events detected at San Emidio in December 2016. Most of the detected events occurred during the plant shutdown (shaded interval) when the power plant was shut down and all pumping ceased. Vertical axis shows the logarithm of the semblance, a measure of coherent seismic energy, as measured by passive seismic emission tomography (PSET) [Warren et al., 2018].

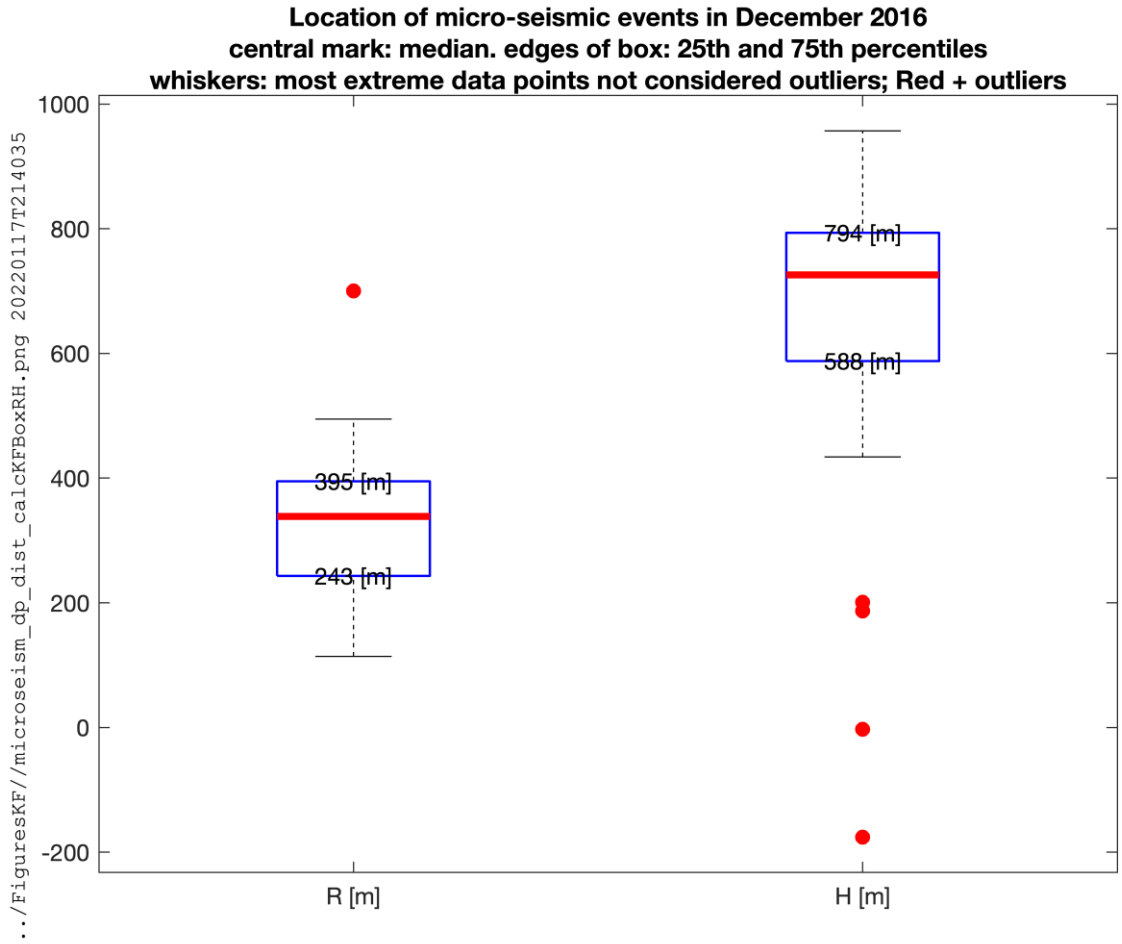

Figure 15. Distributions of distance *R* to nearest well [m] and elevation *H* [masl] and microseismic events observed in December 2016. In these "box and whisker" plots, the red central mark denotes the median. The bottom and top edges of each box denote the 25th and 75th percentiles, respectively. The whiskers denote the most extreme data points not considered outliers. The red circles denote outliers.

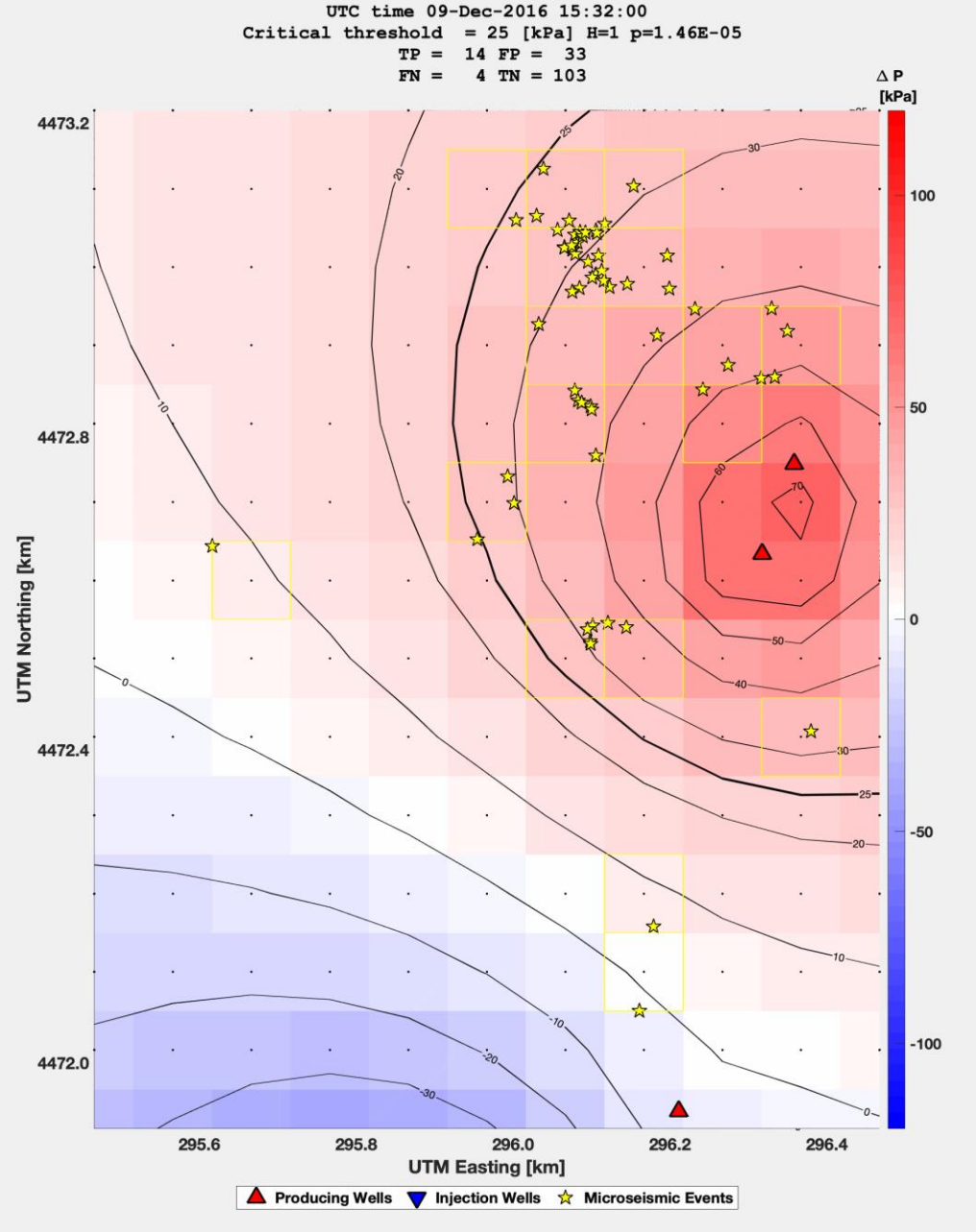

Figure 16 Analytical solution [*Theis*, 1935] for pore pressure changes on a 2D field in response to the shutdown of reservoir operations in December 2016. The map shows the modeled change in pressure calculated for a time 19.5 hours after all pumping ceased. Blue shading indicates decreases in pore pressure and red shading indicates increases in pore pressure. Observed locations of microseismic events are shown by yellow stars. This model assumes a diffusivity value of 112 m^2/s. For this example, the critical threshold of 25 kPa is assumed. The width of each square cell in the grid is 100 m. Red, upward pointing triangles show producing wells; blue, downward pointing triangles, injection wells. Coordinates are Easting and Northing in meters in the Universal Transverse Mercator (UTM) projection, such that tick marks are separated by 500 meters. Figure and caption [Cardiff, Roland, et al., manuscript in preparation].

2 x 2 contingency table

Modeled?	Observed ? Yes: Bins with event detected	Observed ? No: Bins with no event detected	Totals
Yes: Modeled pressure Increase > $\Delta P_{critical}$	52	1689	**1741**
No: Modeled pressure Increase < $\Delta P_{critical}$	8	4411	**4419**
Totals	**60**	**6100**	**p≅10^{-21}**

Figure 17. Contingency table showing the number of microseismic events during the plant shutdown in December 2016. For each cell in a spatiotemporal grid, we calculate the change in fluid pressure using the 2-D analytic solution of Theis. If the modeled change in pressure exceeds the critical ("threshold") value of 25 kPa, then we count that bin in the upper row of the table. If a microseismic event was detected in a cell, then we count that cell in the left column of the table. Each cell is 100 meters by 100 meters in map view and 30 minutes in temporal duration. Following Cardiff et al. [2019], we apply Fisher's nonparametric test for contingency tables [*Fisher*, 1922]. The null hypothesis of conditional independence, i.e., that there is no significant difference in the variable distribution ("event detected") between the rows (describing the modeled pressure). For the data presented, the value of the test statistic (the odds ratio) is 17, where an odds ratio of unity implies independence. The associated p-value is well below a 1% threshold ($P \sim 10^{-21}$), meaning that the null hypothesis of independence can be rejected with greater than 99% confidence. We therefore infer that increasing pore-fluid pressure favors local microseismicity.

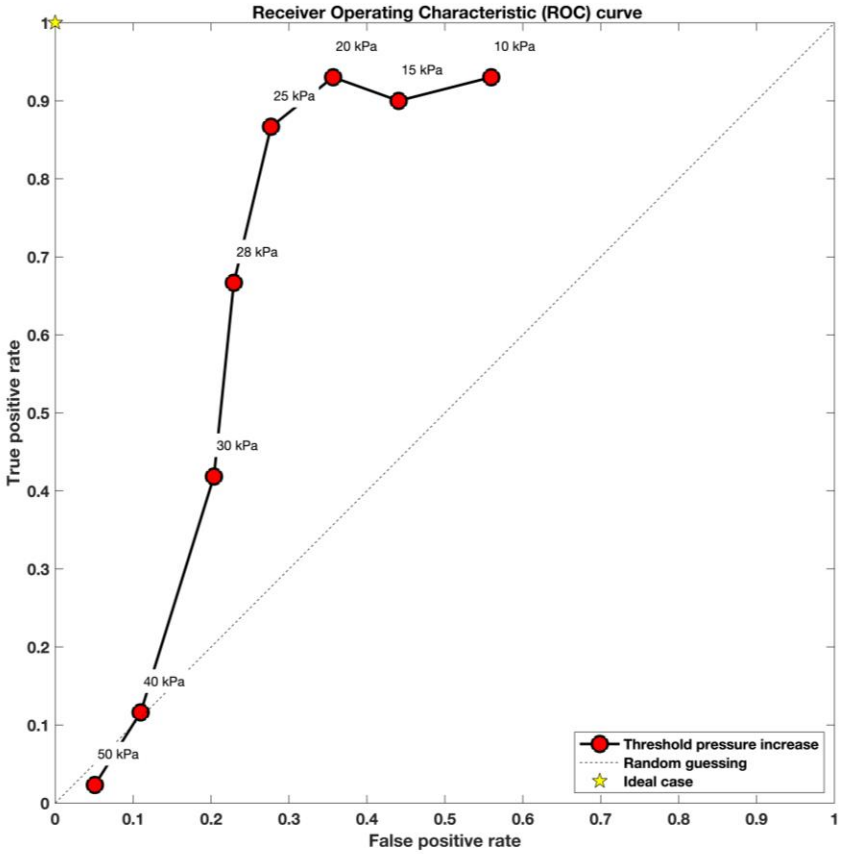

Figure 18. Receiver operating characteristic (ROC) curve, showing the true positive rate against the false positive rate at various settings for the critical ("threshold") value of the modeled increase in pressure.

REFERENCES

Bayuk, I. O., M. Ammerman, and E. M. Chesnokov (2008), Upscaling of elastic properties of anisotropic sedimentary rocks, Geophysical Journal International, 172, 842-860. https://doi.org/10.1111/j.1365-246X.2007.03645.x

Blewitt, G., W. C. Hammond, and C. Kreemer (2018), Harnessing the GPS Data Explosion for Interdisciplinary Science, Eos, 99. https://doi.org/10.1029/2018EO104623

Brodsky, E. E., and L. J. Lajoie (2013), Anthropogenic Seismicity Rates and Operational Parameters at the Salton Sea Geothermal Field, Science. http://dx.doi.org/10.1126/science.1239213

Cardiff, M., D. D. Lim, J. R. Patterson, J. Akerley, P. Spielman, J. Lopeman, . . . K. L. Feigl (2018), Geothermal production and reduced seismicity: Correlation and proposed mechanism, Earth and Planetary Science Letters, 482, 470-477. https://doi.org/10.1016/j.epsl.2017.11.037

Ellsworth, W. L. (2013), Injection-induced earthquakes, Science, 341, 1225942. http://www.ncbi.nlm.nih.gov/pubmed/23846903

Feigl, K. L., and L. M. Parker (2019), PoroTomo Final Technical Report: Poroelastic Tomography by Adjoint Inverse Modeling of Data from Seismology, Geodesy, and Hydrology, Medium: ED; Size: 176 p. pp, ; Univ. of Wisconsin, Madison, WI (United States). https://www.osti.gov/servlets/purl/1499141

Kleich, S. J., M. Folsom, J. Hampton, K. F. Feigl, and WHOLESCALE_Team (2022), Lab-scale structural analysis and poroelastic measurements of rocks from the San Emidio Geothermal Field, Nevada, U.S., paper presented at 45th Workshop on Geothermal Reservoir Engineering, February 7-9, 2022, Stanford University, Stanford, California,.

Kreemer, C., G. Blewitt, and P. Davis (2020), Geodetic evidence for a buoyant mantle plume beneath the Eifel volcanic area, NW Europe, Geophysical Journal International, 222., 1316-1332. https://doi.org/10.1093/gji/ggaa227

Kwiatek, G., P. Martínez-Garzón, G. Dresen, M. Bohnhoff, H. Sone, and C. Hartline (2015), Effects of long-term fluid injection on induced seismicity parameters and maximum magnitude in northwestern part of The Geysers geothermal field, Journal of Geophysical Research: Solid Earth, 120, 7085-7101. https://agupubs.onlinelibrary.wiley.com/doi/abs/10.1002/2015JB012362

Majer, E. L., R. Baria, M. Stark, S. Oates, J. Bommer, B. Smith, and H. Asanuma (2007), Induced seismicity associated with enhanced geothermal systems, Geothermics, 36, 185-222.

McGarr, A., B. Bekins, N. Burkardt, J. Dewey, P. Earle, W. Ellsworth, . . . A. Sheehan (2015), Coping with earthquakes induced by fluid injection, Science, 347, 830-831. http://www.sciencemag.org/content/347/6224/830.full.pdf

NRC (2013), Induced Seismicity Potential in Energy Technologies, National Acad. Press, Washington, D. C.

Patterson, J. R., M. Cardiff, T. Coleman, H. Wang, K. L. Feigl, J. Akerley, and P. Spielman (2017), Geothermal reservoir characterization using distributed temperature sensing at Brady Geothermal Field, Nevada, The Leading Edge, 36, 1024a1021 - 1024a1027. http://dx.doi.org/10.1190/tle36121024a1.1

Raleigh, C. B., J. H. Healy, and J. D. Bredehoeft (1976), An experiment in earthquake control at rangely, colorado, Science, 191, 1230-1237. http://www.ncbi.nlm.nih.gov/pubmed/17737698

Reinisch, E. C., M. Cardiff, and K. L. Feigl (2018), Characterizing Volumetric Strain at Brady Hot Springs, Nevada, USA Using Geodetic Data, Numerical Models, and Prior Information, Geophysical Journal International, 1501–1513. http://dx.doi.org/10.1093/gji/ggy347

Reinisch, E. C., M. Cardiff, C. Kreemer, J. Akerley, and K. L. Feigl (2020), Time-series Analysis of Volume Change at Brady Hot Springs, Nevada, USA using Geodetic Data from 2003 – 2018, Journal of Geophysical Research: Solid Earth, n/a, e2019JB017816. http://dx.doi.org/10.1029/2019jb017816

Rhodes, G. T. (2011), Structural controls of the San Emidio Geothermal System, M.S. thesis, vi, 73 leaves pp, University of Nevada Reno advisor).

Rhodes, G. T., J. E. Faulds, and A. R. Ramelli (2011), Preliminary Geologic Map of the Northern Lake Range, San Emidio Geothermal Area, Washoe County, Nevada, Nevada Bureau of Mines and Geology. http://data.nbmg.unr.edu/public/freedownloads/of/of2011-11.zip

Segall, P., and S. Lu (2015), Injection-induced seismicity: Poroelastic and earthquake nucleation effects, Journal of Geophysical Research: Solid Earth, 120, 5082-5103. http://dx.doi.org/10.1002/2015jb012060

Trugman, D. T., P. M. Shearer, A. A. Borsa, and Y. Fialko (2016), A comparison of long-term changes in seismicity at The Geysers, Salton Sea, and Coso geothermal fields, Journal of Geophysical Research: Solid Earth, 121, 225-247. http://dx.doi.org/10.1002/2015jb012510

Warren, I., E. Gasperikova, S. Pullammanappallil, S. S, and M. Grealy (2018), Mapping Geothermal Permeability Using Passive Seismic Emission Tomography Constrained by Cooperative Inversion of Active Seismic and Electromagnetic Data, paper presented at Proceedings, 43rd Workshop on Geothermal Reservoir Engineering Stanford University, Stanford, California, 2018 SGP-TR-213, February 12-14, 2018. https://pangea.stanford.edu/ERE/pdf/IGAstandard/SGW/2018/Warren.pdf